Materials Today 97 (2026) 103333

Contents lists available at ScienceDirect

Materials Today

journal homepage: www.elsevier.com/locate/mattod

Dual-metal-sites decoupling ionic transport and mechanical reinforcement in hybrid interface toward stable sodium metal batteries

Enzhong Jin [a,1], Hongyu Hou [b,1], Ying Zhao [c,1], Yijia Wang [a], Parham Pirayesh [a], Chao Zhang [a], Yi Yuan [a], Yi Gan [a], Guerman Popov [d], Lyudmila V. Goncharova [d], Ruirui Zhang [a], Frederick Benjamin Holness [a], Sanaz Ketabi [e], Fang Dai [e], Jun Song [c,***], Changhong Cao [b,**], Yang Zhao [a,*]

[a] Department of Mechanical and Materials Engineering, University of Western Ontario, London, Ontario N6A 5B9, Canada
[b] Department of Mechanical Engineering, McGill University, Montreal, Quebec H3A 0C3, Canada
[c] Department of Mining and Materials Engineering, McGill University, Montreal, Quebec H3A 0C3, Canada
[d] Department of Physics and Astronomy, University of Western Ontario, London, ON N6A 3K7, Canada
[e] General Motors Research and Development Center, Harley Earl Boulevard, Warren, MI 48092, USA

A B S T R A C T

Sodium (Na) metal batteries (NMBs) offer great potential for high-energy–density storage applications. However, their practical use remains constrained by persistent challenges such as Na dendrite growth and interfacial instability. In this work, we design and fabricate a dual-metal-sites crosslinked polymer interface on Na metal anodes, which synergistically integrates sodiophilic sites, rapid interfacial kinetics, and enhanced mechanical crosslinking. This nanoscale hybrid interface features a tunable composition, optimized sodiophilicity, and exceptional mechanical stiffness, effectively suppressing dendrite propagation and stabilizing Na deposition. Electrochemical evaluations demonstrate that the dual-metal-sites hybrid interface enables unprecedented cycling stability under high-capacity operation. Complementary insights from electro-chemo-mechanical DFT modeling and mechanistic experiments reveal that the dual-metal synergy decouples ionic transport from mechanical degradation, facilitating homogeneous Na^+ flux and adaptive SEI reconfiguration. By combining sodiophilic functionality with robust polymer–metal coordination, this work establishes a universal design strategy for durable, dendrite-free metal anodes, advancing the development of next-generation energy storage technologies.

Introduction

The global transition toward electrified mobility and grid-scale renewable energy integration has propelled unprecedented demand for advanced energy storage systems. Even though lithium (Li)-ion batteries (LIBs) dominate modern energy storage landscapes, powering applications ranging from portable electronics to electric vehicles (EVs), their scalability is constrained by geopolitical lithium supply risks, soaring material costs, and inherent sustainability challenges [1,2]. Due to its abundance and its comparable chemistry during operation, Na batteries have emerged as one of the most promising candidates for next-generation energy storage. Unfortunately, the energy density of sodium (Na)-ion batteries (NIBs) is insufficient to meet the demands of modern energy storage systems. In this regard, Na metal batteries (NMBs) are particularly attractive because of the high theoretical specific capacity (1166 mAh g^{-1}), low electrochemical redox potential (−2.71 V versus the standard hydrogen electrode), and low density (0.97 g cm^{-3} at 20 °C) of Na metal anode [3]. However, the practical application of Na metal anodes is limited by several serious challenges driven by three interrelated interfacial issues. (i) The high reactivity of Na fosters electrolyte decomposition, forming a mechanically fragile solid electrolyte interphase (SEI) prone to break during cycling, perpetuating parasitic SEI regeneration and electrolyte depletion [2]. (ii) SEI thickening increases ionic transport barriers and induces volumetric strain, accelerating capacity fade [4]. (iii) Finally, due to defects and uneven SEI composition, electrochemical heterogeneity across the electrode surface causes localized current concentration triggering dendrite formation and growth and eventual cell failure [5]. Therefore, an ideal SEI is

* Corresponding author.
** Corresponding author.
*** Corresponding author.
E-mail addresses: jun.song2@mcgill.ca (J. Song), changhong.cao@mcgill.ca (C. Cao), yzhao628@uwo.ca (Y. Zhao).
[1] +These authors contributed equally to this work.

https://doi.org/10.1016/j.mattod.2026.103333
Received 5 February 2026; Received in revised form 20 March 2026; Accepted 11 April 2026
Available online 24 April 2026

critical to ensuring the stable cycling and safety of Na metal anodes, which have chemical/electrochemical stability to prevent parasitic reactions with electrolytes; homogeneous ionic flux and electric field distribution to suppress dendrites formation; and mechanical robustness to accommodate Na plating/stripping induced volume changes without fracture [6].

To achieve these goals and suppress dendrite growth, various effective strategies have been widely explored, such as designing advanced structural hosts, introducing functional electrolyte additives, and engineering SEIs [7–9]. Among these, interface stabilization strategies for Na metal anodes predominantly focus on engineered artificial interfaces, including inorganic, organic, and composite layers [10–16]. While organic coatings excel in flexibility, their inherently low stiffness (<1 GPa) limits interfacial durability even if higher than the natural-formed SEI layer (585 MPa), whereas purely inorganic layers often sacrifice strain tolerance for rigidity. Hybrid interfaces, combining the mechanical flexibility of organic components with the structural rigidity and ionic conductivity of inorganic phases, have emerged as highly promising candidates. For instance, hybrid organic–inorganic protective films, such as PVDF-HFP-Al_2O_3 [17], PVDF-NaF [18], PVDF-ZnF_2 [19], PMMA/graphene [20] and $SnCl_2$-PCMX [15], leverage in situ reactions during cycling to form mechanically robust phases. For example, during cycling, Na reacts with PVDF to in situ form Na_2O_2 and NaF with high mechanical strength and ionic conductivity, which facilitates rapid Na^+ migration, as well as PVDF with high flexibility to accommodate volume expansion [21,22]. In addition to reinforcing the mechanical properties, sodiophilic sites for the hybrid interfaces with enhanced Na wettability and reduced nucleation overpotential for stable Na metal deposition are another driving force. Single active sites, such as metals of Sn [23], Co [24] and Bi [25] were applied to stabilize Na nucleation through fully reversible alloying-dealloying reactions, resulting in strong interfacial affinity, reducing nucleation barriers to enable uniform plating [26]. Moreover, adopting Al or Zn metals has emerged as a useful strategy in recent studies. For instance, Al atoms act as strong Lewis-acidic centers that exhibit a competitive affinity for electron-rich solvent molecules, effectively disrupting the Na^+ solvation sheath and lowering the desolvation activation energy [27]. Zn atoms serve as highly sodiophilic sites governed by their specific electronic configuration, reducing the nucleation overpotential through the favorable formation of Na–Zn alloy phases [28]. However, introducing single active sites is insufficient to improve both mechanical stability and sodiophilicity. The quantitative mechanical characterization of such nanolayers remains sparse, and scalable fabrication of mechanically stable nanoscale coatings is still nascent. Although hybrid designs mitigate the brittleness of native SEI, weak interfacial adhesion in these systems compromises Na^+ transport kinetics, which needs cohesive interfaces that harmonize ionic conductivity, mechanical resilience and interfacial compatibility.

In recent years, nanolayers deposited by atomic layer deposition (ALD) or molecular layer deposition (MLD), including inorganic metal oxides (such as ZnO [29], ZrO_2 [30]), organic polymers (such as alucone [31] and polyurea [32]), and metal-infiltrated organic polymers (such as Al-PEO [33]), have been widely adopted for Li/Na metal anodes as artificial SEI layers due to their precise control over thickness and conformity. Although traditional ALD/MLD processes may raise concerns regarding efficiency and cost, these technologies have already been extensively commercialized in the semiconductor industry [34,35]. Furthermore, the rapid development of continuous roll-to-roll and spatial ALD/MLD effectively addresses the high-throughput requirements for large-scale battery manufacturing [36–38]. Importantly, given the nanometer-scale thickness of these conformal coatings, the actual raw material cost per cell is practically negligible, demonstrating the tremendous feasibility of this strategy for practical applications.

Herein, we fabricate a rationally designed nanoscale dual-metal-sites crosslinked hybrid interface for Na metal anodes. The interface incorporates Zn and Al linked with N-rich polyurea (PUEA) chains, where both metals participate in sodiation. The cooperative interactions between Zn and Al couple Na affinity with mechanical robustness, ensuring homogeneous Na^+ flux and dendrite-free deposition even at high areal capacities (up to 5 mAh cm^{-2}). This work presents a transformative approach to stabilizing Na metal anodes through synergistic dual-metal-sites crosslinked polymer interface realizing high-performance and long-life Na-metal batteries.

Results and discussion

To simultaneously enhance interfacial sodiophilicity, optimize Na^+ transport kinetics, and reinforce the mechanical integrity of the PUEA matrix, we incorporated dual metal sites of Zn and Al into a hybrid interface, thereby coupling ionic transport with mechanical robustness (Fig. 1). The hybrid interface with dual-metal sites was deposited by MLD technique. Based on the MLD protocol for pure polyurea, using ethylenediamine (ED) and 1,4-phenylene diisocyanate (PDIC) as precursors, we fabricated a hybrid dual-metal-sites crosslinked PUEA architecture through alternating cycles of Al-PUEA and Zn-PUEA deposition. Comprehensive parameters for MLD process are detailed in the Supplementary Information. The detailed reaction mechanism of the MLD (Zn,Al)PUEA is illustrated in Fig. S1. The fabrication process involved two sub-cycles. In the first sub-cycle, Al-PUEA was synthesized by introducing trimethylaluminum (TMA) as the Al crosslinker. This involved a reaction between TMA and ED, forming dative Al-N bonds, followed by the formation of urea bonds via the reaction between the isocyanate groups of PDIC and the amine groups of ED [39,40]. In the second sub-cycle, Zn-PUEA is synthesized by introducing diethylzinc (DEZ) as the crosslinker. A direct ligand-exchange reaction occurs between the ethyl ligands of DEZ and the terminal —NH_2 groups of the preceding Al-PU layer, forming covalent Zn—N bonds [41]. The dual-metal-sites crosslinked PUEA interface was constructed by alternately combining these two sub-groups (Al-PUEA and Zn-PUEA), resulting in a layered structure denoted as x(TMA-ED-PDIC-ED)-y(DEZ-ED-PDIC-ED) (x:y = 1:1, 1:2, 2:1), where x and y denote the number of sequential deposition cycles applied to the Al-PUEA and Zn-PUEA sub-cycles, respectively. This approach could sufficiently control the compositions and ratio of two metal sites of Al and Zn in the nanoscale hybrid interface. For instance, a ratio of x:y = 1:2 corresponds to one cycle of Al-PUEA deposition (TMA-ED-PDIC-ED) followed by two cycles of Zn-PUEA deposition (DEZ-ED-PDIC-ED) within a single composite layer.

In-situ quartz crystal microbalance (QCM) analysis reveals the growth dynamics of dual-metal-sites PUEA interphases, demonstrating linear mass gain dependence on deposition time with selected periodic steps (Fig. S2). For (Zn,Al)PUEA, each MLD cycle exhibits a total mass increase of $\Delta m_{(Zn,Al)PUEA} \approx 131$ ng cm^{-2}, dominated by the mass gain of TMA ($\Delta m_{TMA} \approx 75$ ng cm^{-2}) and PDIC, while DEZ contributes a minority ($\Delta m_{DEZ} \approx 2.0$ ng cm^{-2}) (Fig. S2a). In (2Zn,Al)PUEA, sequential DEZ exposures yield $\Delta m_{DEZ} \approx 1.0$ ng cm^{-2} (first pulse) and 3.0 ng cm^{-2} (second pulse), with TMA dominant mass gain contributions ($\Delta m_{TMA} \approx 74$ ng cm^{-2}) and a total cycle mass gain of $\Delta m_{(2Zn,Al)PUEA} \approx 172$ ng cm^{-2} (Fig. S2b). For (Zn,2Al)PUEA, dual TMA pulses ($\Delta m_{TMA} \approx 70.0$ ng cm^{-2} and 64.0 ng cm^{-2}) drive a total mass increase of $\Delta m_{(Zn,2Al)PUEA} \approx 206.4$ ng cm^{-2}, while DEZ still remains minor ($\Delta m_{DEZ} \approx 1.0$ ng cm^{-2}) (Fig. S2c). QCM results indicate the majority of mass contribution is from TMA and PDIC exposure, DEZ contributes to a minor part of mass growth. The dual-metal-sites crosslinked PUEA interface was synthesized via MLD with varying cycle numbers (5, 10, 25, 50) to modulate thickness and compositional uniformity. Samples are systematically labelled as Na-nDMC(xZn,yAl)PUEA (dual-metal-sites crosslinked, DMC), where n represents the total MLD cycles. For instance, a sample fabricated with 25 total MLD cycles and a Zn: Al ratio of 2:1 is named as Na-25DMC(2Zn,Al)PUEA.

The surface morphology and elemental distribution of the Na-10DMC(Zn,Al)PUEA electrode prior to electrochemical cycling were initially investigated via top-view scanning electron microscopy (SEM) and energy-dispersive X-ray spectroscopy (EDX). The SEM images reveal

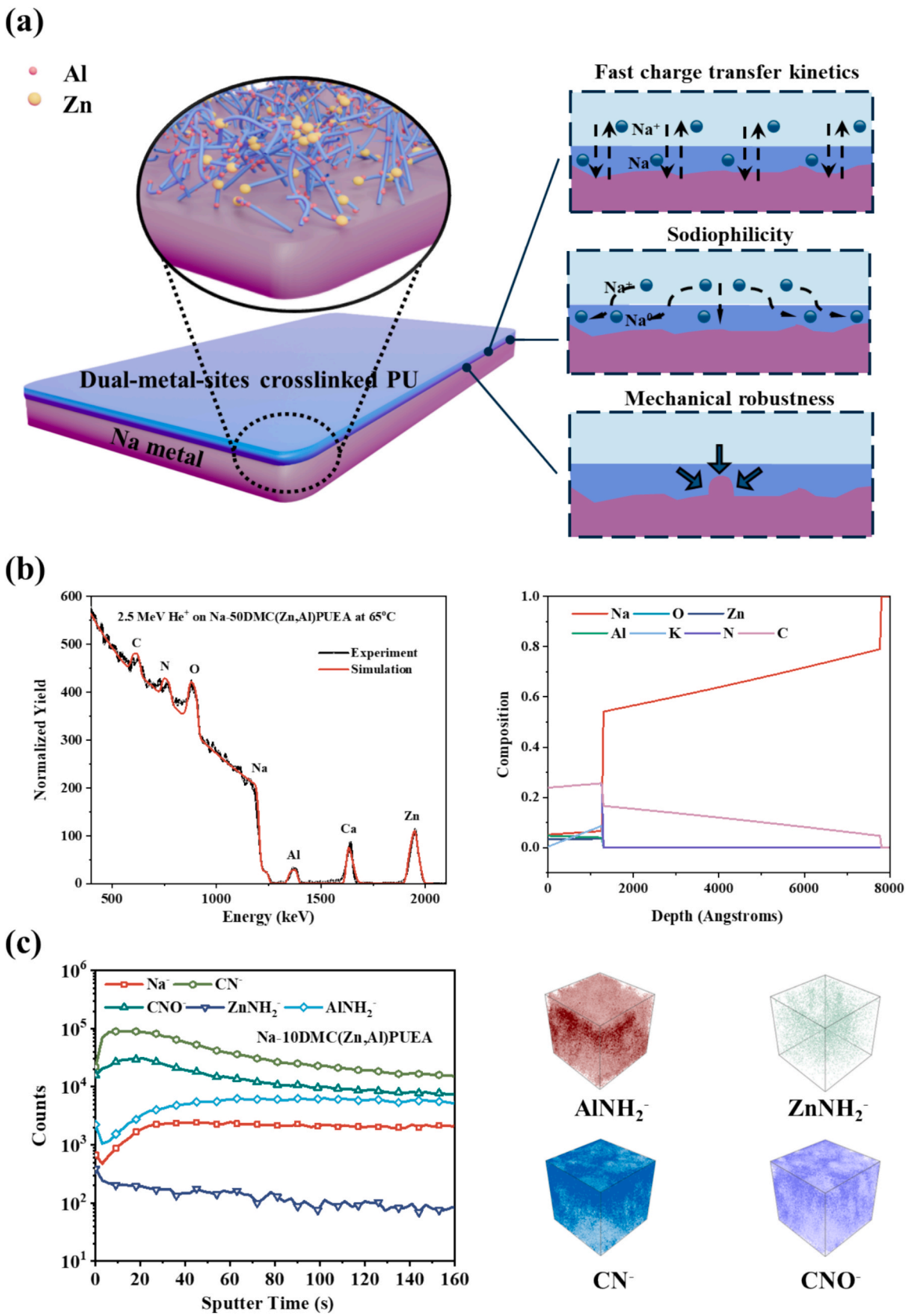

Fig. 1. (a) Schematic illustration of dual-metal-sites crosslinked PUEA hybrid interface structure on Na metal. (b) The RBS spectra and simulated depth profiles of Na-50DMC(Zn,Al)PUEA. (c) The ToF-SIMS depth profile of various secondary ion species and corresponding 3D rendering images of Na-10DMC(Zn,Al)PUEA.

that the dual-metal-sites crosslinked PUEA layer provides a relatively uniform and conformal coverage across the sodium foil surface (Fig. S3a). Spatially resolved EDX elemental mapping further corroborates the successful integration of the hybrid interface, showcasing a homogeneous distribution of Zn, Al and N throughout the surface (Fig. S3b). While some inherent surface features are visible, they are primarily attributed to the initial roughness of the bulk Na and minor oxidation during the sample transfer process.

To investigate the thickness and chemical compositions of the artificial interface, Rutherford backscattering spectrometry (RBS) measurements were performed on Na-10DMC(Zn,Al)PUEA and Na-50DMC (Zn,Al)PUEA. The RBS spectrum and corresponding simulation profiles (Fig. 1b) reveal the presence of N, Al, and Zn at the surface, confirming the existence of dual-metal-sites crosslinked PUEA layers. Moreover, the Ca signal is derived from the impurity in bulk Na and a prominent O peak is observed, which can be attributed to air exposure of the Na-50DMC(Zn,Al)PUEA foil during sample transfer. It is noteworthy that the signals for Al and Zn in Na-10DMC(Zn,Al)PUEA are weak due to the ultra-thin coating thickness (Fig. S4), as the (Zn,Al)PUEA coating thickness decreases, there are substantially less of these elements present. In the fitting results of the depth profile of Na-50DMC(Zn,Al)PUEA, the decline in the signals of coating elements (N, Al and Zn) and a concurrent increase in the Na signal at ~120 nm indicates the coating layer thickness. It is worth noting that the Na foil surface was oxidized during transfer, leading to increased surface roughness which made the RBS thickness measurements imprecise.

The structure and composition of artificial interface were further examined by time-of-flight secondary ion mass spectrometry (ToF-SIMS) and were presented by the depth profile corroborating the distribution of specific components on the Na metal surface (Fig. 1c). $ZnNH_2^-$ and $AlNH_2^-$ ions are derived from Zn and Al crosslinkers in the PUEA chains, respectively, while CNO^- and CN^- ions originate from the urea bonds within the PUEA matrix. As sputter time increases, secondary ions from species located deeper beneath the surface are detected. The counts for CN^- and CNO^- ions reach a peak within the first ~20 s of Cs^+ sputtering and subsequently decrease to a plateau. The relatively low initial intensity of $AlNH_2^-$ and $ZnNH_2^-$ signals, which subsequently reach a stable stage, further corroborates the homogeneous dispersion of these metals within the PUEA matrix, which also can be observed from 3D rendering images (Fig. 1c). The signal intensity differences between $AlNH_2^-$ and $ZnNH_2^-$ in ToF-SIMS results are consistent with the relative intensities of Al and Zn determined by RBS. In parallel, the Na^- signal remains negligible in the early stages but rises gradually within ~20 s, indicating the transition from the coating layer to the Na metal substrate through sputtering. Moreover, the depth profiles of Na-25DMC(Zn,2Al)PUEA (Fig. S5a) exhibit similar trends to those of Na-10DMC(2Zn,Al)PUEA (Fig. S5b). The $AlNH_2^-$ and AlO_2^- signals in Na-25DMC(Zn,2Al)PUEA gradually increase during the initial ~80 s of sputtering, reaching a plateau at ~100 s. In contrast, the $ZnNH_2^-$ signal remains stable for the first ~20 s, then decreases until about 100 s, after which it levels off into a stable plateau. For Na-10DMC(2Zn,Al)PUEA, the Al^- signal intensity progressively ascends to a maximum at ~200 s of sputtering followed by a decay, while the $ZnNH_2^-$ fragment shows a continuous decline, stabilizing to a plateau beyond ~200 s. Depth profile results reveal a significantly lower crosslink efficiency for Zn precursor versus Al, as shown by the attenuated secondary ion counts of Zn secondary ions fragments compared to their Al counterparts. This disparity in dopant integration kinetics results in dual-metal content within the PUEA coating that deviates from the designed stoichiometric ratio. However, it is worth mentioning that ToF-SIMS results are only semiquantitative because of the matrix effects, surface roughness of Na foil and sample oxidation during the transfer [42].

To understand the interfacial chemistry and composition of dual-metal-sites crosslinked PUEA hybrid interface, X-ray photoelectron spectroscopy (XPS) on Na-10DMC(Zn,Al)PUEA was performed (Fig. S6a-d). The C 1s spectrum (Fig. S6a) reveals four binding components: C—H/C—C (284.8 eV), C═C (283.0 eV), C═O (288.0 eV) and C—N (286.3 eV) which correspond to the bonding configurations of the polymer chain backbone which are consistent with previously reported literature [43,44]. The chemical bonding configuration between C and N is further validated by the N 1s spectrum (Fig. S6b). A predominant N—C═O at 399.8 eV from urea functional groups and a minor component N═C at ~398.0 eV are assigned to isocyanate terminal groups from the PDIC [43]. In the Al 2p spectrum (Fig. S6c), the peak at 74.1 eV is attributed to Al in the + 3 oxidation state, thereby confirming the presence of Al-based crosslinkers [45]. Zn 2p spectrum (Fig. S6d) shows Zn in the polymer film is +2 oxidation state (Zn $2p_{3/2}$ at ~1021 eV and Zn $2p_{1/2}$ at ~1044 eV). The XPS results indicate that both Al and Zn exist in oxidized states, suggesting strong coordination interactions between the metal centers and the polyurea matrix. These interactions involve partial electron withdrawal from the metal atoms toward the coordinating O/N atoms. However, the spatially dispersed Zn 2p XPS signals corroborate the trace-amount Zn content within the interface. This result is consistent with the Zn-depleted region identified in the RBS simulated depth profile (Fig. 1b), the trace $ZnNH_2^-$ signals ($< 10^3$ counts) resolved by ToF-SIMS mapping (Fig. 1c) and in-situ QCM analysis results (Fig. S2).

Beyond chemical composition, the electronic transport kinetics within the artificial interface are pivotal in determining its passivating efficacy. To investigate this, the electronic conductivities (σ_e) of the DMC(Zn,Al)PUEA, Zn,PUEA and pure PUEA coatings were quantified using the Hebb-Wagner polarization method (Fig. S7a and Table S2) [46]. The DMC(Zn,Al)PUEA interface exhibited a suppressed σ_e of 6.90×10^{-13} S cm^{-1} (Fig. S7b), representing lower reduction compared to pristine PUEA (6.10×10^{-11} S cm^{-1}) (Fig. S7d) and lower than the Zn, PUEA interface σ_e of 6.59×10^{-12} S cm^{-1} (Fig. S7c). It indicates that the synergistic effect of the Zn-Al dual-metal crosslinking effectively densifies the polymer matrix and eliminates continuous electronic leakage pathways, which is a critical prerequisite for long-term interfacial stability and dendrite-free growth.

To evaluate the cycling stability of Na metal anodes determine the optimal dual-metal sites ratio and thickness of nanolayers, symmetric cells were fabricated using pristine or coated Na electrodes. Fig. S8 presents the electrochemical performance of Na-nDMC(Al,Zn)PUEA, Na-nDMC(2Al,Zn)PUEA, and Na-nDMC(Al,2Zn)PUEA with different layer thicknesses in symmetrical cells. All cells were cycled at a high current density of 10 mA cm^{-2} with a capacity cutoff of 1 mAh cm^{-2}. In the (Zn,Al)PUEA group (Fig. S8a), the Na@10(Zn,Al)PUEA configuration demonstrates exceptional cycling stability, maintaining a low voltage of ≈ 0.1 V (vs. Na^+/Na) for 180 h in the range of 5–50 MLD cycles. Conversely, for the (2Zn,Al)PUEA group (Fig. S8b), while Na-50DMC(2Zn,Al)PUEA initially achieves lower polarization (0.08 V) for 60 h, voltage fluctuations emerge beyond 80 h, whereas Na-25DMC (2Zn,Al)PUEA sustains stable voltage (0.1 V) over 100 h, reflecting improved stress dissipation at intermediate thicknesses. Within the (Zn,2Al)PUEA group (Fig. S8c), Na-10DMC(Zn,2Al)PUEA demonstrates better electrochemical stability with voltage deviation (± 0.13 V) over 60 h. The above results identify the Na-10DMC(Zn,Al)PUEA electrode as the optimal configuration, showing optimal electrochemical stability and longest cycle lifetime (>180 h) under ultra-high current density conditions. Furthermore, to elucidate this optimal performance, both thickness and ratio-composition dependent electrochemical impedance spectroscopy (EIS) measurements were conducted (Fig. S9 and Fig. S10). The unsodiated coatings act primarily as physical barriers before cycling. Consequently, the initial interfacial charge-transfer resistance (R_{ct}) increases from 5 to 50 MLD cycles (Fig. S9a), while remaining similar among the 10-cycle configurations with different metal ratios due to their similar physical thickness (Fig. S10a). However, the properties of the electrochemically sodiated interfaces emerge after cycling. Regarding thickness, the overly thin 5-cycle coating exhibits a massive impedance increase indicating interfacial failure, whereas thicker coatings (25–50 cycles) maintain high impedance because the elongated diffusion path severely restricts Na^+ transport kinetics (Fig. S9b).

Regarding the various metal ratio within the optimal 10 cycle thickness, the (Zn,Al)PUEA ratio maintains the lowest R_{ct} (Fig. S10b). In contrast, the (Zn,2Al)PUEA interface suffers from sluggish kinetics due to insufficient sodiophilic Zn sites, while the (2Zn,Al)PUEA interface undergoes mechanical degradation due to a lack of robust Al crosslinking sites. As a result, the (Zn,Al)PUEA coating achieves the ideal synergistic balance, simultaneously decoupling ionic transport limitations from mechanical degradation.

To benchmark the performance enhancements afforded by dual-metal-sites, a comparative electrochemical analysis was conducted among the optimized dual-metal-sites crosslinked PUEA on Na electrodes, single Zn metal crosslinked PUEA (Na-10Zn,PUEA) and bare Na (Fig. 2). When the current density is 1 mA cm^{-2} with a capacity of 3 mAh cm^{-2}, bare Na exhibits rapid interfacial degradation, with voltage

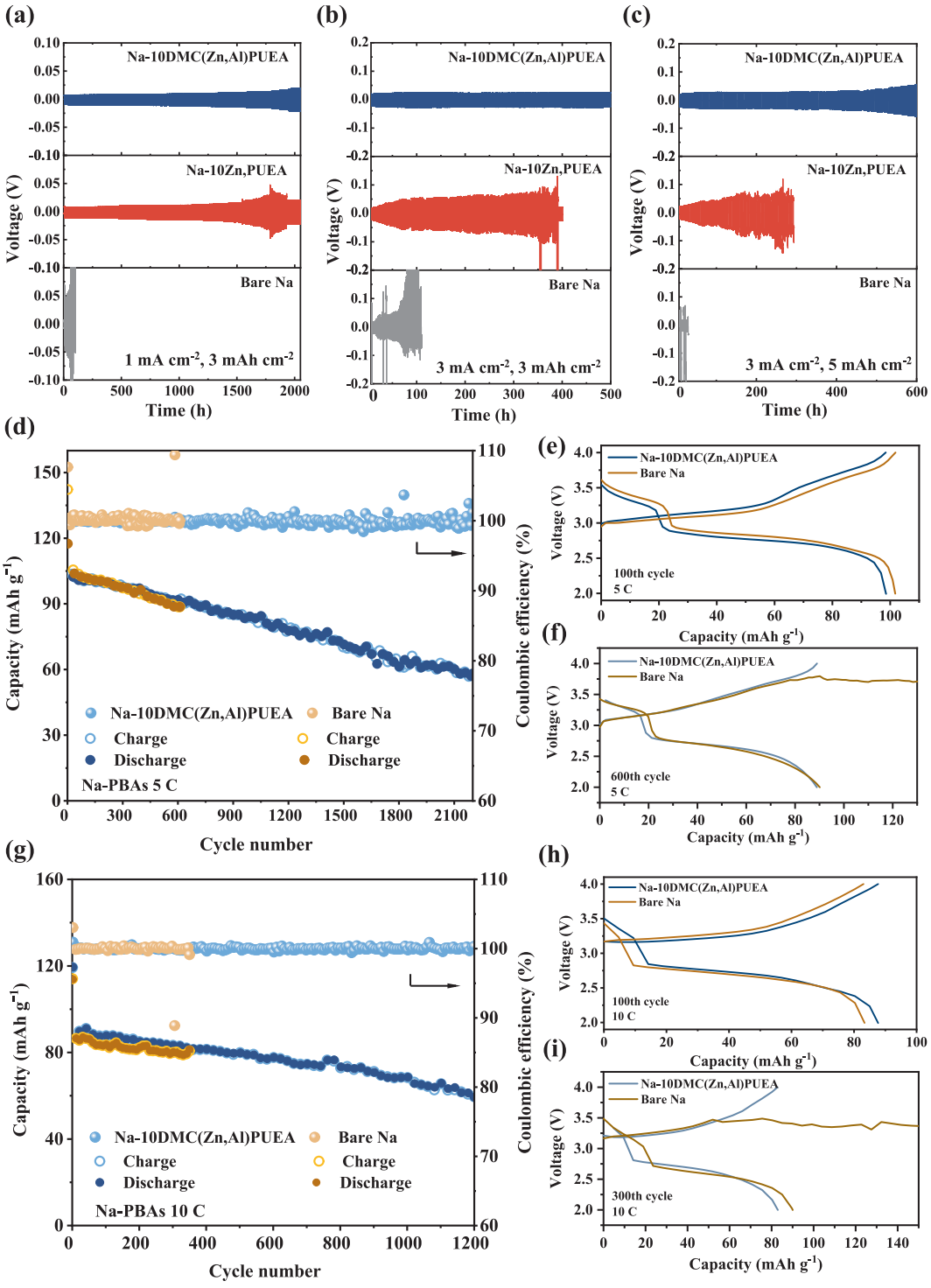

Fig. 2. Cycling stability of symmetrical cells with bare Na, Na-10Zn,PUEA and Na-10DMC(Zn,Al)PUEA using ether-based electrolyte at a current density of (a) 1 mA cm^{-2} with cut-off capacity of 3 mAh cm^{-2}, (b) 3 mA cm^{-2} with cut-off capacity of 3 mAh cm^{-2} and (c) 3 mA cm^{-2} with cut-off capacity of 5 mAh cm^{-2}. Cycling performance of Na-PBAs full cells with the bare Na and the Na-10DMC(Zn,Al)PUEA anodes at a rate of (d) 5C, (g) 10C (1C represents 170 mA g^{-1}) and their corresponding galvanostatic charge–discharge profile at (e, f) 5C and (h, i) 10C.

polarization exceeding 100 mV within 90 h due to uncontrolled dendrite growth and parasitic electrolyte decomposition (Fig. 2a). In contrast, Na-10DMC(Zn,Al)PUEA shows exceptional cyclability, maintaining an ultralow overpotential (±18 mV) for over 2000 h, has a longer lifetime and is more stable than single-metal Na-10Zn,PUEA (24 mV, 1700 h). At a current density of 3 mA cm^{-2} and a capacity density of 3 mAh cm^{-2} (Fig. 2b), the single-metal Na-10Zn,PUEA exhibits voltage oscillations (±75 mV) for 350 h, followed by abrupt polarization collapse (−0.2 V vs. Na^+/Na), indicative of soft short-circuit formation. In contrast, the Na-10DMC(Zn,Al)PUEA maintains a stable run over 500 h with minimal voltage deviation (±25 mV). Remarkably, even under extreme conditions of 3 mA cm^{-2}, 5 mAh cm^{-2}, Na-10DMC(Zn,Al)PUEA sustains ultralow hysteresis (± 50 mV) over 600 h, where the single-metal system rapidly degrades into erratic voltage fluctuations (± 50 mV) after 130 h (Fig. 2c).

To validate the universality of the dual-metal PUEA strategy, its application was extended to solid-state Na metal batteries using Na_3SbS_4 (NAS) solid-state electrolyte. The room-temperature ionic conductivity of NAS is measured as 1.1 × 10^{-3} S cm^{-1} (Fig. S11). Based on optical dual-metal ratio liquid cells, symmetric cells were assembled with the optimal Zn:Al stoichiometric ratio (1:1) across varying nanolayer thicknesses (n = 5, 10, 25, 50 MLD cycles) (Fig. S9). At 0.3 mA cm^{-2} and 0.1 mAh cm^{-2}, Na-10DMC(Zn,Al)PUEA electrode showed exceptional interfacial stability, with a gradual overpotential increase from ± 0.58 V (at 50 h) to ± 2.0 V (at 300 h), achieving the longest cycle life (>300 h), compared to other samples which suffered rapid polarization escalation due to interfacial failure and dendrite growth (Fig. S12a). Even under severe conditions (0.3 mA cm^{-2}, 0.3 mAh cm^{-2}), Na-10DMC(Zn,Al)PUEA maintained stable operation for over 250 h (Fig. S12b). Collectively, these results indicate the Na-10DMC(Zn,Al)PUEA configuration as the universally optimal architecture for Na metal batteries, achieving unparalleled stability across both liquid and solid-state systems through dual-metal synergy. To validate the effectiveness of the coating layer compared with single-metal crosslinked PUEA under solid-state conditions, symmetric cells with Na-10DMC(Zn,Al)PUEA, Na-10Zn,PUEA and bare Na were tested using the NAS electrolyte (Fig. S13). Both crosslinked PUEA electrodes showed substantially reduced polarization compared to bare Na, demonstrating that the hybrid coating slightly mitigates interfacial degradation in solid-state Na cells. The electrochemical performance of symmetric cells employing artificial SEI layers for Na metal anodes, as reported in previous studies, is summarized in Table S1 for comparison.

To evaluate the practical viability of dual-metal-sites crosslinked PUEA-protected Na metal anodes in full cell configurations, NMBs with Prussian blue analogue (PBA) cathodes were assembled. Both bare Na and Na-10DMC(Zn,Al)PUEA||PBA cells were cycled at 5C and 10C to assess interfacial stability (Fig. 2d–i). The PBA cathode delivered initial discharge specific capacity of 119.4 mAh g^{-1} with an initial Coulombic efficiency (ICE) of around 100 %. At 5 C, the Na-10DMC(Zn,Al)PUEA cell delivered charge–discharge capacities comparable to the bare Na counterpart, (Fig. 2d). Na-10DMC(Zn,Al)PUEA cell maintained a high capacity of 80.75 mAh g^{-1} after 2100 cycles with high-capacity retention of 57.8 %, whereas the bare Na exhibited an abrupt increase in charge capacity at 600th cycle indicative of severe dendritic growth (Fig. 2e and f). Under 10 C cycling, both cells initially achieved similar capacities (~91 mAh g^{-1}). However, at 300th cycle, the bare Na||PBA cell displayed pronounced oscillations in charge capacity alongside persistently low Coulombic efficiency (CE) (Fig. 2 g and i), revealing exacerbated dendrite growth and intermittent soft short-circuiting at the anode interface. In contrast, the Na-10DMC(Zn,Al)PUEA||PBA full cell sustained a stable charge–discharge capacity of 68.56 mAh g^{-1} at 1000 cycle with capacity retention of 74.73 % (Fig. 2h). The full cell results corroborate the results from symmetric cell testing, confirming that the Na-10DMC(Zn,Al)PUEA interface critically enhances overall capacity stability through stabilizing Na^+ electrodeposition and suppressing interfacial degradation even at ultra-high C-rates.

To comprehensively probe the interfacial electrochemical properties, more electrochemical characterization tests were employed. EIS was conducted to investigate the interfacial charge transfer kinetics of the SEIs. Nyquist plots of pristine symmetric cells (before cycling) reveal impedance profiles for Na-10DMC(Zn,Al)PUEA, Na-10Zn,PUEA, and bare Na (Fig. 3a). The Na-10DMC(Zn,Al)PUEA cell exhibits a charge-transfer resistance (R_{ct} ≈ 13 Ω), which is higher than that of bare Na (R_{ct} ≈ 12 Ω). This higher initial interfacial resistance can be attributed to the highly dense artificial SEI layer. Prior to cycling, this dense metal crosslinked polymer layer has not yet undergone electrochemical sodiation, whereas bare Na relies only on a spontaneously formed native SEI which stems from reaction with liquid electrolyte. However, the Na-10Zn,PUEA sample exhibits the lowest initial resistance. This is attributed to the lower crosslinking efficiency of the Zn precursor, resulting in a less dense network that is rapidly permeated by the electrolyte and provides sodiophilic sites.

Further study of the electrochemical nucleation kinetics and energy barriers governing initial Na deposition were obtained via galvanostatic plating in half-cells using Cu substrates fabricated by dual-metal-sites crosslinked PUEA hybrid interface of varying ratios and optimized MLD cycles. Na nucleation initiates exclusively when embryonic nuclei exceed the critical radius (R_{crit}) defined as: [47]

$$R_{crit} = \frac{2\gamma_{NE}V_m}{F|\eta_n|}$$

where η_n represents the nucleation overpotential on a current collector. The discharge profile (Fig. 3b) exhibited an initial voltage drop (SEI formation) followed by two critical characteristic overpotentials: (1) nucleation overpotential (η_n) reflecting the energy barrier for heterogeneous nucleation; (2) the plateau potential (η_p) corresponding to sustained Na growth. The Cu-10DMC(Zn,Al)PUEA electrode demonstrated the lowest η_n, correlating with an increased R_{crit} that suppresses high-density, disordered nucleation. Furthermore, the minimal potential gap between η_n and η_p (15 mV) indicates reduced electrochemical supersaturation, enabling stable Na nuclei formation while overcoming a minimal energy barrier. Thus, the 10(Zn,Al)PUEA interface with more sodiophilic sites results in a lower nucleation density, leading to a more controlled nucleation process that promotes uniform Na deposition. Interfacial charge transfer kinetics and mass transport properties of the artificial SEI layers were quantitatively evaluated via Tafel analysis derived from cyclic voltammetry in Na symmetric cells (Fig. 3c). The exchange current density J_0 were calculated from the data of Tafel plots for each cell shown in Fig. 3d, which are 5.74, 2.84 and 0.43 mA cm^{-2} for the Na-10DMC(Zn,Al)PUEA, Na-10Zn,PUEA and bare Na, respectively. The high J_0 value of Na-10DMC(Zn,Al)PUEA anode indicates the fast charge transfer at the electrode/electrolyte interface, delivering a faster mass transfer than that of Na-10Zn,PUEA and bare Na [48–50].

To further elucidate the Na^+ transport mechanism through the dual-metal crosslinked PUEA interlayer, Temperature-dependent EIS was conducted on the symmetric cell of Na-10DMC(Zn,Al)PUEA (Fig. S14a). Based on the Arrhenius equation, the symmetric cell exhibits the activation energy E_a of 27.92 kJ mol^{-1} (Fig. S14b). This value aligns with the typical energy barrier range (20–30 kJ mol^{-1}) reported for rapid ion-hopping mechanisms in polymer-based electrolytes [51,52]. This energy barrier suggests that Na^+ migration through the PUEA interlayer is primarily governed by a coordination-site hopping mechanism, coupled with localized polymer segmental dynamics [53]. Particularly, the abundant terminal groups (such as C=O and N–H) within the polyurea chains act as affinitive hopping sites which can lower the desolvation energy of Na^+ and facilitate rapid ion transport across the interface, ensuring uniform Na^+ flux and suppressing dendrite nucleation [54].

The morphological evolution and interfacial integrity of the Na-10DMC(Zn,Al)PUEA electrode following cycling were tested via post-mortem SEM and EDX analysis. As shown in Fig. 4a, the top-view SEM image of bare Na reveals a rough surface with a heterogeneous

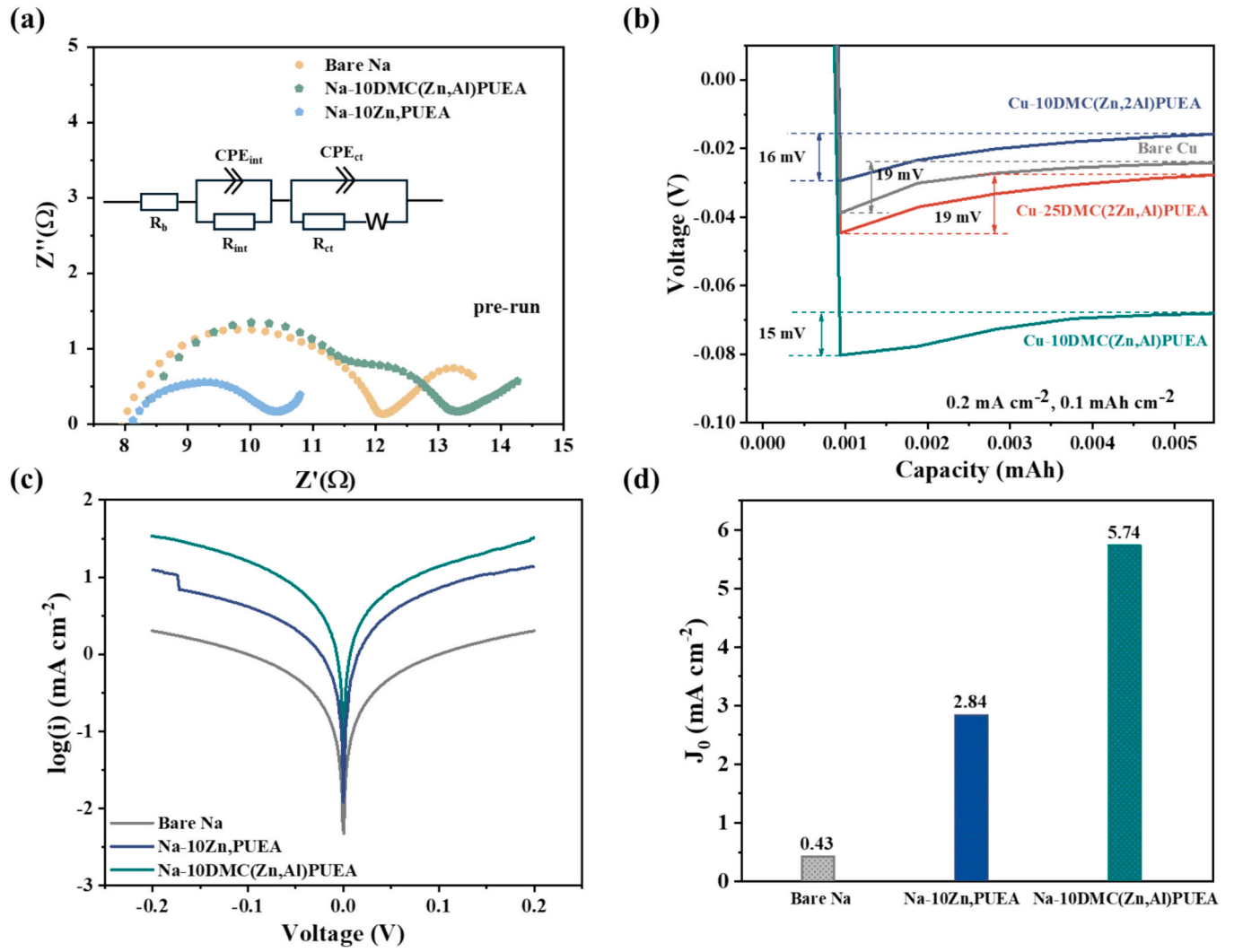

Fig. 3. (a) Nyquist plot of symmetrical cells of Na-10Zn,PUEA, Na-10DMC(Zn,Al)PUEA and bare Na before cycling. (b) Detailed nucleation curves of Na deposition on Cu foils with different coatings. (c) Tafel plot and (d) corresponding exchange current density of Na symmetrical cells with 10Zn,PUEA, 10(Zn,Al)PUEA and bare Na.

distribution of spherical features. This 'mossy' structure indicates uncontrolled volume expansion and non-uniform plating/stripping processes, which inherently trigger interfacial polarization and dendritic failure. In contrast, the surface of Na-10DMC(Zn,Al)PUEA is considerably smoother and flatter, with no evidence of mossy or uneven spherical formations, indicating the stabilizing effect of the dual-metal-sites crosslinked PUEA hybrid interface (Fig. 4b and Fig. S15a). Spatially resolved SEM-EDX mapping on the cycled anode revealed that the signature elements (Al, N and Zn) of the artificial interface were uniformly distributed across the surface region (Fig. S15b). This dual-metal-sites crosslinked architecture successfully confines Na growth and prevents direct contact between the active Na and the electrolyte, effectively suppressing parasitic side reactions and ensuring stable, dendrite-free over cycling.

The morphological evolution of Na nucleation during electrodeposition was investigated via SEM for bare Cu and Cu-10DMC(Zn,Al)PUEA current collectors under galvanostatic plating at 0.5 mA cm^{-2} with incremental areal capacities (0.1, 0.5, 1.0 mAh cm^{-2}). At 0.1 mAh cm^{-2}, localized Na aggregated as irregular spherical nuclei onto bare Cu and it partially covered the electrode surface with Na deposits (Fig. S16a), reflecting heterogeneous nucleation dominated by high interfacial energy barriers. As the capacity increases to 0.5 mAh cm^{-2}, pervasive cracks form on the surface of bare Cu, culminating in a porous, non-uniform morphology at 1.0 mAh cm^{-2}. However, the Cu-10DMC(Zn,Al)PUEA substrate demonstrates spatially uniform Na deposition at all stages (Fig. S16b), with no observable Cu exposure. The artificial SEI interface further maintains planar Na growth, confirming its efficacy in stabilizing plating dynamics. To elucidate whether Na^+ deposits penetrate through the artificial SEI layer or nucleate directly on top of the coating, the Cu-10DMC(Zn,Al)PUEA substrate was examined for Na plating. The spatial distribution of deposited Na was analyzed using SEM-EDX to visualize the interfacial deposition patterns. From the top-view EDX mapping, distinct signals of Al, N, and Zn were clearly detected on the Na-deposited regions, indicating that Na plating occurred beneath the coating layer rather than on its surface (Fig. S17).

To study the interfacial evolution, EIS and ToF-SIMS were performed again on cycled symmetric cells (30 cycles) of Na-10DMC(Zn,Al)PUEA, Na-10Zn,PUEA, and bare Na. Post-cycling EIS (Fig. 4c) reveals that once sodiation, the DMC(Zn,Al)PUEA layer establishes conductive Na^+ transport pathways, dropping the R_{ct} of the coated electrode to the 1 Ω. In contrast, the bare Na interface suffers catastrophic degradation. Uncontrolled volumetric expansion repeatedly ruptures the fragile native SEI, leading to rampant dendrite growth and the continuous accumulation of 'dead' Na, which causes the R_{ct} of bare Na to surge to 300 Ω. ToF-SIMS depth profiling (Fig. 4d) reveals interfacial component change in cycled Na-10DMC(Zn,Al)PUEA anodes. Fragments associated with

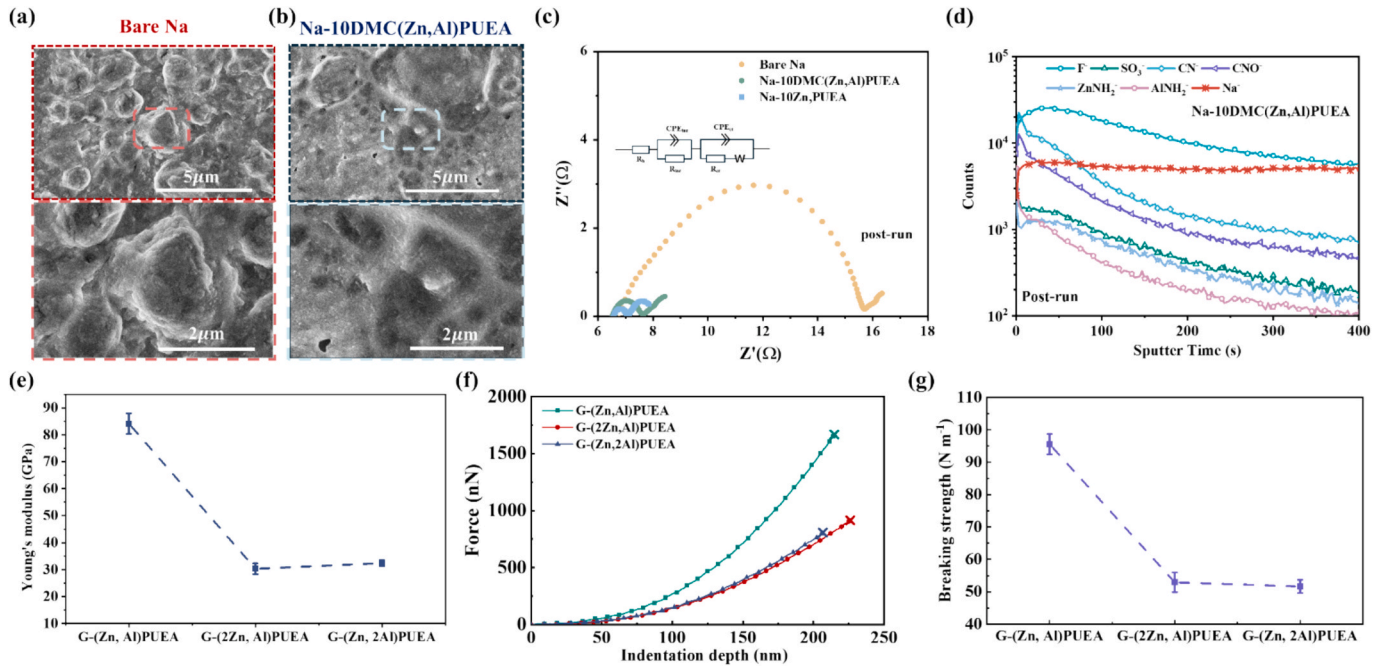

Fig. 4. Top-view SEM images of (a) bare Na and (b) Na-10DMC(Zn,Al)PUEA after electrochemical cycling (30 cycles). (c) Nyquist plot of Na symmetrical cells with 10Zn,PUEA, 10(Zn,Al)PUEA and bare Na after cycling (30 cycles). The inset is the overall profile of bare Na. (d) ToF-SIMS secondary ion depth profiles of Na-10DMC (Zn,Al)PUEA after electrochemical cycling (30 cycles). Dual-metal-site crosslinked PUEA with different metal ratios deposited on monolayer graphene measured from atomic force microscopy (AFM) deflection tests: (e) Young's modulus, (f) representative force–indentation depth (F–δ) curves from the AFM deflection tests to capture the breaking forces of the nanofilms (marked crosses indicate the points of failure) and (g) two-dimensional breaking strength.

the polymer matrix (CN^-, CNO^-) and metal coordination ($ZnNH_2^-$, $AlNH_2^-$) show similar attenuation from the top surface, plateauing after 400 s of Cs^+ sputtering (Fig. 4d). Notably, $AlNH_2^-$ intensity declined, indicating partial dissolution of Al crosslinked PUEA into the electrolyte. Despite comparable initial F^- intensities of Na-10(Zn,Al)PUEA and bare Na (Fig. S18), the dual-metal-sites crosslinked PUEA interface suppresses F^- accumulation, attributed to its ability to hinder $SO_3CF_3^-$ electrolyte to further corrode through the anode surface.

The mechanical properties of the polyurea nanofilms were evaluated using atomic force microscopy (AFM) deflection tests on films deposited on monolayer graphene supported on perforated transmission electron microscopy (TEM) grids, denoted as G-DMC(Zn,Al)PUEA, G-DMC(2Zn, Al)PUEA, and G-DMC(Zn,2Al)PUEA, respectively. This experiment method enables reliable suspended-film measurements in the few-nanometer thickness regime where conventional techniques such as nanoindentation are dominated by substrate effects rather than the film response. We acknowledge that this configuration does not replicate the rough morphology of Na metal foils and therefore does not provide an absolute measurement of the coating properties under realistic battery conditions. Instead, our objective is to obtain a comparative assessment of the elasticity and fracture strength of different PUEA films with varying Al-Zn crosslinker ratios under identical deposition and testing conditions. In this suspended geometry, the polyurea films consist of tens of molecular layers, making their thickness and volume fraction substantially larger than that of the monolayer graphene support (~0.34 nm), so that the overall stiffness and strength are dominated by the polymer layer, as also suggested in previous polymer/graphene thin-film studies [55,56]. Firstly, low-load (≤ 200nN) elastic deflection tests were carried out at over ten different locations of each sample. Elastic moduli and breaking strength were calculated by fitting the experimentally obtained force–displacement curves into a classic mechanics model (Fig. S19 and Eq. S2). The results in Fig. 4e revealed that the average Young's modulus of G-DMC(Zn,Al)PUEA (84.1 ± 3.8 GPa) is significantly higher than those of the other two cases: 30.3 ± 2.0 GPa for G-DMC(2Zn,Al)PUEA and 32.4 ± 1.1 GPa for G-DMC(Zn,2Al)PUEA, and consistently higher than that of pure PUEA coating (4.7–5.9 GPa for G-50PUEA measured previously [45]). The higher Young's modulus of G-DMC(Zn,Al)PUEA suggests a more rigid molecular framework, which enhances charge transfer by maintaining structural integrity under operation. After the initial elastic deflection tests, multiple deflection-to-failure tests were also performed. As shown by the representative fracture curves in Fig. 4f, the G-DMC(Zn,Al)PUEA demonstrates the highest breaking force (1582.4 ± 104.0 nN), outperforming the other cases: G-DMC(2Zn,Al)PUEA (940.3 ± 105.0 nN) and G-DMC(Zn,2Al)PUEA (812.0 ± 62.8 nN). Converting breaking forces to two-dimensional strengths (Eq. S3), G-DMC(Zn,Al)PUEA (95.6 ± 3.1 N m^{-1}) film is still the strongest among the three and the other two cases have similar strength levels: 52.9 ± 3.0 N m^{-1} for G-DMC(2Zn,Al)PUEA and 51.6 ± 2.0 N m^{-1} for G-DMC(Zn,2Al)PUEA (Fig. 4g). The higher breaking strength allows G-DMC(Zn,Al)PUEA to better accommodate volume expansion/contraction during sodiation–desodiation cycles. While the differences in both modulus and strength for G-DMC(2Zn,Al)PUEA and G-DMC(Zn,2Al)PUEA are small, the AFM characterizations demonstrate that mechanical properties of metal-PUEA nanofilms can be tailored by varying the ratio of Al and Zn crosslinkers in the PUEA matrix. This compositional control over fracture resistance and elasticity provides a design idea for optimizing artificial SEI nanolayers on Na metal anode.

To elucidate the role of Al and Zn linkers, DFT calculations were conducted to analyze Na adsorption on PUEA-PUEA (linker-free), PUEA-Al-PUEA, and PUEA-Zn-PUEA. The results indicate that Na has a strong tendency to form bonds with oxygen (O) (Fig. 5a-f). When Na is positioned directly next to O, only minor structural deformation occurs (Fig. 5a, c and e). However, if Na is placed near atoms adjacent to O, the chain undergoes considerable distortion, facilitating bond formation between Na and O (Fig. 5b, d, f). Notably, regardless of chain deformation, the presence of linkers leads to higher adsorption energies (E_{ads}) compared to the linker-free case of PUEA-PUEA. Among these, PUEA-Al-PUEA exhibits the highest E_{ads} of − 0.98 eV when distortion occurs, along with increased charge transfer from Na to O (Optimized structure shown in Fig. S20). The high adsorption energies when incorporating

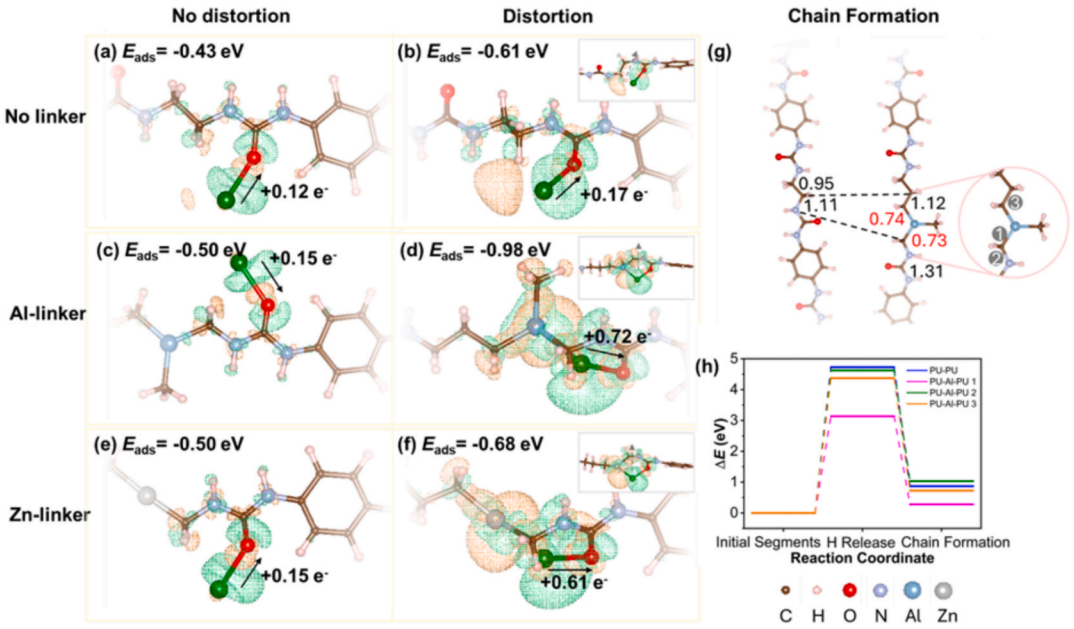

Fig. 5. (a-f) Na adsorption on PUEA-PUEA, PUEA-Al-PUEA, and PUEA-Zn-PUEA with charge density isosurfaces. The green isosurface represents the negative charge density difference of -10^{3}e Bohr^{-1}, while the orange isosurface represents the positive charge density difference of $+10^{-3}$e Bohr^{-1}. (g) Chain formation energies of PUEA-PUEA and PUEA-Al-PUEA. (h) Bond order near the chain connection points in PUEA-PUEA and PUEA-Al-PUEA.

the linkers indicate that the introduction of Al linker promotes stable Na adsorption, facilitating Na deposition. While the highly negative Na adsorption energy of the Al site is beneficial for initial Na^+ adsorption, such an excessively sodiophilic interface can potentially act as a 'kinetic trap' based on the Sabatier principle for metal battery anode [57]. Excessively strong binding severely hinders the subsequent desorption and hopping diffusion of Na^+ through the polymer matrix. By introducing trace Zn as a chemical modulator, the local electronic environment of the polymer backbone is subtly tuned. This effectively mitigates the strong Al-Na interaction, achieving a moderate binding affinity that prevents Na^+ trapping and facilitates rapid capture-release dynamics. This strategic balance between affinity and transport kinetics leads to the good performance of the DMC(Zn,Al)PUEA interface. By synergistically incorporating Zn with Al, the DMC(Zn,Al)PUEA interface achieves an optimized sodiophilic sites that promotes rapid charge transfer. An optimal adsorption strength is critical in polymer electrolytes: overly weak interactions hinder Na^+ solvation and transport, whereas excessively strong binding immobilizes the ions, impairing diffusion [58]. This theoretical dual-metal kinetic regulation corroborates high exchange current density (J_0) of 5.74 mA cm^{-2} (Fig. 3d), accelerating the interfacial charge transfer compared to the Zn-crosslinked or bare Na anodes.

Given that Na adsorption is more favorable on deformed structures with higher adsorption energies, we propose that the structural deformability plays a key role in enabling such favorable configurations. To investigate the effect of linkers on the mechanical deformability of PUEA chains, bond order and chain formation energy analysis were performed for PUEA-PUEA and PUEA-Al-PUEA systems (Fig. 5g and h). The bond order reflects the strength of the bond connecting PUEA units, while the chain formation energy quantifies the energy required to assemble the segments (i.e., PUEA-PUEA or PUEA-Al-PUEA). Full methodological details are provided in the simulation section of the Supplementary Information. The bond order results reveal that the introduction of an Al linker replaces the stronger N-C bond in PUEA-PUEA (bond order ≈ 1.11) with two weaker Al-C bonds (bond order ≈ 0.74). This weakening is also reflected in the chain formation energies (Fig. 5h), which decrease upon linker introduction. The chain formation process involves two steps, starting with hydrogen desorption from the initial segments (PUEA and/or TMA) followed by chain assembly. Note that for Al-linked PUEA, three possible chain formation pathways exist depending on the binding site, as shown in the inset of Fig. 5g. As seen from Fig. 5h, PUEA-PUEA exhibits the highest formation energy, while Al-linked configurations, especially at site 1 (Al-C bond), require less energy. The above results indicate that the Al crosslinker facilitates the formation of the PUEA chains, while at the same time introducing weaker Al-C bonds to replace the otherwise direct N-C bonds connecting PUEA units. This enables easier structural rearrangements toward lower-energy configurations during Na adsorption, which contributes to improved sodiophilicity of the system.

Conclusion

In this study, we have successfully demonstrated the effectiveness of dual-metal-sites crosslinked polymer coatings in fabricating a stable artificial SEI for high-performance Na metal anodes. By precisely controlling the film composition through MLD, we developed dual-metal-sites crosslinked PUEA coatings, specifically DMC(Zn,Al)PUEA with enhanced stiffness and improved sodiophilic properties. This artificial interface enabled the stable operation of Na metal anodes at high areal capacities (5 mAh cm^{-2}) with only a negligible increase in overpotential, effectively suppressing dendrite growth. DFT simulations reveal that the introduction of metal linkers enhances Na adsorption by enabling structural deformation, allowing the system to access lower-energy configurations favorable for Na adsorption. Overall, our findings demonstrate the promising potential of dual-metal-sites crosslinked PUEA coatings to provide robust sodiophilic sites and mechanically stable interface, offering a viable pathway for the design and fabrication of next-generation high-performance energy storage systems and advancing Na metal anode battery technologies closer to practical applications.

CRediT authorship contribution statement

Enzhong Jin: Writing – original draft, Validation, Methodology, Investigation, Formal analysis, Data curation, Conceptualization. **Hongyu Hou:** Writing – original draft, Investigation, Formal analysis, Data

curation. **Ying Zhao:** Writing – original draft, Investigation, Formal analysis, Data curation. **Yijia Wang:** Writing – review & editing, Investigation, Formal analysis. **Parham Pirayesh:** Writing – review & editing, Investigation, Formal analysis. **Chao Zhang:** Writing – review & editing, Investigation, Formal analysis. **Yi Yuan:** Writing – review & editing, Methodology, Formal analysis. **Yi Gan:** Writing – review & editing, Methodology, Formal analysis. **Guerman Popov:** Writing – review & editing, Methodology, Formal analysis. **Lyudmila V. Goncharova:** Writing – review & editing, Methodology, Formal analysis. **Ruirui Zhang:** Writing – review & editing, Formal analysis. **Frederick Benjamin Holness:** Writing – review & editing, Formal analysis. **Sanaz Ketabi:** Writing – review & editing, Funding acquisition. **Fang Dai:** Writing – review & editing, Funding acquisition. **Jun Song:** Writing – review & editing, Supervision, Methodology, Formal analysis, Data curation. **Changhong Cao:** Writing – review & editing, Supervision, Methodology, Formal analysis. **Yang Zhao:** Writing – original draft, Investigation, Formal analysis, Data curation.

Declaration of competing interest

The authors declare that they have no known competing financial interests or personal relationships that could have appeared to influence the work reported in this paper.

Acknowledgments

Y. Zhao acknowledges support from the Natural Sciences and Engineering Research Council of Canada (NSERC), the Canada Foundation for Innovation (CFI), Canada, the Ontario Research Fund (ORF), Canada, Mitacs, and Carbon Solutions, a Strategic Priorities Fund project of the University of Western Ontario (UWO), Canada. C. Cao acknowledges support from the Natural Sciences and Engineering Research Council of Canada through a Discovery Grant (NSERC RGPIN-2021-02664) and a Nova Grant (ALLRP 597993-24). J. Song acknowledges support from the Natural Sciences and Engineering Research Council of Canada through a Discovery Grant (NSERC RGPIN-2023-03628). Computational resources were provided by the Digital Alliance of Canada.

Appendix A. Supplementary data

Supplementary data to this article can be found online at https://doi.org/10.1016/j.mattod.2026.103333.

Data availability

Data will be made available on request.

References

[1] S. Zheng, et al., Ionogel-based sodium ion micro-batteries with a 3D Na-ion diffusion mechanism enable ultrahigh rate capability, Energ. Environ. Sci. 13 (3) (2020) 821–829.
[2] C. Chu, et al., Recent advanced skeletons in sodium metal anodes, Energ. Environ. Sci. 14 (8) (2021) 4318–4340.
[3] P. Pirayesh, et al., Na metal anodes for liquid and solid-state Na batteries, Energ. Environ. Sci. 17 (2) (2024) 442–496.
[4] E. Matios, et al., Enabling safe sodium metal batteries by solid electrolyte interphase engineering: a review, Ind. Eng. Chem. Res. 58 (23) (2019) 9758–9780.
[5] F. Huang, et al., In-depth understanding of interfacial na^{+} behaviors in sodium metal anode: migration, desolvation, and deposition, Adv. Mater. 36 (41) (2024).
[6] M. Mandl, et al., Sodium metal anodes: Deposition and dissolution behaviour and SEI formation, Electrochim. Acta 354 (2020) 136698.
[7] K. Wang, et al., Enabling high-performance sodium metal anodes by 2D nanomaterials engineering: a review, Mater. Today Energy 42 (2024) 101565.
[8] J. Luo, et al., Stabilizing sodium metal anodes with surfactant-based electrolytes and unraveling the atomic structure of interfaces by Cryo-TEM, Nano Lett. 22 (3) (2022) 1382–1390.
[9] J. Luo, et al., Tunable MXene-derived 1D/2D hybrid nanoarchitectures as a stable matrix for dendrite-free and ultrahigh capacity sodium metal anode, Nano Lett. 20 (10) (2020) 7700–7708.
[10] X. Zhou, et al., Heterogeneous interfacial layers derived from the in situ reaction of CoF2 nanoparticles with sodium metal for dendrite-free na metal anodes, Adv. Energy Mater. 12 (42) (2022) 2202323.
[11] E. Jin, et al., Ionic conductive and highly-stable interface for alkali metal anodes, Small 18 (33) (2022) e2203045.
[12] P. Pirayesh, et al., From nanoalloy to nano-laminated interfaces for highly stable alkali-metal anodes, Adv. Mater. 35 (29) (2023) e2301414.
[13] M. Zhu, et al., Dendrite-free sodium metal anodes enabled by a sodium benzenedithiolate-rich protection layer, Angew. Chem. 132 (16) (2020) 6658–6662.
[14] C. Wang, et al., Robust anode-free sodium metal batteries enabled by artificial sodium formate interface, Adv. Energy Mater. 13 (22) (2023).
[15] P. Liu, et al., Inorganic–organic hybrid multifunctional solid electrolyte interphase layers for dendrite-free sodium metal anodes, Angew. Chem. Int. Ed. 62 (47) (2023).
[16] J. Luo, et al., Pillared MXene with Ultralarge interlayer spacing as a stable matrix for high performance sodium metal anodes, Adv. Funct. Mater. 29 (3) (2019) 1805946.
[17] Y.-J. Kim, et al., Enhancing the cycling stability of sodium metal electrodes by building an inorganic–organic composite protective layer, ACS Appl. Mater. Interfaces 9 (7) (2017) 6000–6006.
[18] S. Wang, et al., An implantable artificial protective layer enables stable sodium metal anodes, ACS Appl. Energy Mater. 3 (9) (2020) 8688–8694.
[19] K. Yu, et al., Artificial solid-electrolyte interphase with PVDF-ZnF2 double-layer structures enhancing electrochemical performance of sodium metal batteries, Batteries Supercaps (2025).
[20] H. Wang, et al., Critical role of ultrathin graphene films with tunable thickness in enabling highly stable sodium metal anodes, Nano Lett. 17 (11) (2017) 6808–6815.
[21] Y. Liu, et al., Recent developments in interface engineering strategies for stabilizing sodium metal anodes, Cell Rep. Phys. Sci. 5 (5) (2024) 101965.
[22] Z. Hou, et al., Poly(vinylidene difluoride) coating on Cu current collector for high-performance Na metal anode, Energy Storage Mater. 24 (2020) 588–593.
[23] F. Xu, et al., Atomic Sn–enabled high-utilization, large-capacity, and long-life Na anode, Sci. Adv. 8 (19) (2022).
[24] Y. Li, et al., Single cobalt atoms decorated N-doped carbon polyhedron enabled dendrite-free sodium metal anode, Small Methods 5 (11) (2021) 2100833.
[25] S. Zhou, et al., Single-atom engineering for synergistic nucleation and interfacial regulation enabling durable anode-free sodium metal batteries, Adv. Mater. (2025).
[26] L. Zhang, et al., Bi nanoparticles embedded in 2D carbon nanosheets as an interfacial layer for advanced sodium metal anodes, Small 17 (12) (2021) 2007578.
[27] R. Zhang, et al., Strong lewis acid effect in the pores of metal–organic framework host for dendrite-free lithium deposition and stripping, Adv. Mater. 37 (41) (2025).
[28] T. Yang, et al., Mega high utilization of sodium metal anodes enabled by single zinc atom sites, Nano Lett. 19 (11) (2019) 7827–7835.
[29] R. Zhang, et al., Atomic layer deposition assisted superassembly of ultrathin ZnO layer decorated hierarchical Cu foam for stable lithium metal anode, Energy Storage Mater. 37 (2021) 123–134.
[30] P.K. Alaboina, et al., In situ dendrite suppression study of nanolayer encapsulated li metal enabled by zirconia atomic layer deposition, ACS Appl. Mater. Interfaces 10 (38) (2018) 32801–32808.
[31] Y. Zhao, et al., Inorganic–organic coating via molecular layer deposition enables long life sodium metal anode, Nano Lett. 17 (9) (2017) 5653–5659.
[32] Y. Sun, et al., A novel organic "Polyurea" thin film for ultralong-life lithium-metal anodes via molecular-layer deposition, Adv. Mater. 31 (4) (2019) 1806541.
[33] R. Shang, et al., Diffusion behavior and kinetics for the vapor phase infiltration of Trimethylaluminum in Poly(ethylene oxide): an in situ quartz crystal microgravimetry study, ACS Appl. Mater. Interfaces 16 (47) (2024) 64907–64915.
[34] R.A. Ovanesyan, et al., Atomic layer deposition of silicon-based dielectrics for semiconductor manufacturing: current status and future outlook, J. Vac. Sci. Technol. A 37 (6) (2019) 060904.
[35] M. Ritala, J. Niinistö, Industrial applications of atomic layer deposition, ECS Trans. 25 (8) (2009) 641–652.
[36] P. Poodt, et al., Spatial atomic layer deposition: a route towards further industrialization of atomic layer deposition, J. Vac. Sci. Technol. A 30 (1) (2012) 010802.
[37] C.-T. Hsieh, et al., Roll-to-roll atomic layer deposition of Titania Nanocoating on thermally stabilizing lithium nickel cobalt manganese oxide cathodes for lithium ion batteries, ACS Appl. Energy Mater. 3 (11) (2020) 10619–10631.
[38] K. Sharma, et al., Spatial atomic layer deposition on flexible porous substrates: ZnO on anodic Aluminum oxide films and Al2O3 on Li ion battery electrodes, J. Vac. Sci. Technol. A 34 (1) (2016) 01A146.
[39] Y. Xu, C.B. Musgrave, A DFT study of the Al2O3 atomic layer deposition on SAMs: effect of SAM termination, Chem. Mater. 16 (4) (2004) 646–653.
[40] S.M. George, B. Yoon, A.A. Dameron, Surface chemistry for molecular layer deposition of organic and hybrid organic−inorganic polymers, Acc. Chem. Res. 42 (4) (2009) 498–508.
[41] M. Mäkinen, K. Laasonen, Modelling of growth reaction pathways of zincone ALD/MLD hybrid thin films: a DFT study of precursor screening and the diethyl zinc pulse, RSC Adv. 15 (21) (2025) 16299–16311.
[42] S.-K. Otto, et al., In-depth characterization of lithium-metal surfaces with XPS and ToF-SIMS: toward better understanding of the passivation layer, Chem. Mater. 33 (3) (2021) 859–867.
[43] K. Che, et al., Investigations on aging behavior and mechanism of polyurea coating in marine atmosphere, Materials 12 (21) (2019) 3636.

[44] H. Shinohara, et al., XPS and NEXAFS studies of VUV/O 3 -treated aromatic polyurea and its application to microchip electrophoresis, IET Nanobiotechnol. 5 (4) (2011) 136–142.
[45] E. Jin, et al., Electro-chemo-mechanically stable and Sodiophilic interface for na metal anode in liquid-based and solid-state batteries, Adv. Mater. 36 (35) (2024) e2406837.
[46] M.H. Hebb, Electrical conductivity of silver Sulfide, J. Chem. Phys. 20 (1) (1952) 185–190.
[47] H. Wang, et al., Combining theories and experiments to understand the sodium nucleation behavior towards safe sodium metal batteries, Chem. Soc. Rev. 49 (12) (2020) 3783–3805.
[48] Z. Peng, et al., Enhanced stability of Li metal anodes by synergetic control of nucleation and the solid electrolyte interphase, Adv. Energy Mater. 9 (42) (2019) 1901764.
[49] S. Liu, et al., Bulk nanostructured materials design for fracture-resistant lithium metal Anodes, Adv. Mater. 31 (15) (2019) 1807585.
[50] W. Zhao, et al., Engineering sodium metal anode with sodiophilic bismuthide penetration for dendrite-free and high-rate sodium-ion battery, Engineering 11 (2022) 87–94.
[51] C. Gainaru, et al., Mechanisms controlling the energy barrier for ion hopping in polymer electrolytes, Macromolecules 56 (15) (2023) 6051–6059.
[52] M. Patel, et al., A sodium ion conducting gel polymer electrolyte with counterbalance between 1-ethyl-3-methylimidazolium tetrafluoroborate and tetra ethylene glycol dimethyl ether for electrochemical applications, RSC Adv. 14 (20) (2024) 14358–14373.
[53] H. Yue, et al., Rational design of a robust flexible triblock Polyurea copolymer protective layer for high-performance lithium metal batteries, ACS Appl. Mater. Interfaces 14 (50) (2022) 55735–55744.
[54] Y. Xue, X. Li, D.J. Quesnel, Electrochemical and mechanical properties of sodium-ion conducting cross-linked polymer gel electrolyte, Int. J. Electrochem. Sci. 12 (11) (2017) 10674–10686.
[55] J.-Y. Hong, et al., Massachusetts Institute of Technology, MA (US) United States, Cambridge, 2017.
[56] D.G. Papageorgiou, I.A. Kinloch, R.J. Young, Mechanical properties of graphene and graphene-based nanocomposites, Prog. Mater Sci. 90 (2017) 75–127.
[57] J. Zheng, et al., Design principles for heterointerfacial alloying kinetics at metallic anodes in rechargeable batteries, Sci. Adv. 8 (44) (2022).
[58] X. Tang, et al., High-performance quasi-solid-state MXene-based Li–I batteries, ACS Cent. Sci. 5 (2) (2019) 365–373.